

## ARTICLES

Local Structural Studies of  $\text{LiCr}_y\text{Mn}_{2-y}\text{O}_4$  Cathode Materials for Li-Ion Batteries

Mayumi Kaneko,<sup>†</sup> Shinsuke Matsuno,<sup>†</sup> Takeshi Miki,<sup>†</sup> Masanobu Nakayama,<sup>†</sup> Hiromasa Ikuta,<sup>†</sup> Yoshiharu Uchimoto,<sup>†</sup> Masataka Wakihara,<sup>\*,†</sup> and Katsuyuki Kawamura<sup>‡</sup>

Department of Applied Chemistry, Tokyo Institute of Technology, Ookayama, Meguro-ku, Tokyo 152-8552, Japan, and Department of Earth and Planet Science, Tokyo Institute of Technology, Ookayama, Meguro-ku, Tokyo 152-8552, Japan

Received: July 16, 2002; In Final Form: December 7, 2002

The local crystal structure of a spinel-type solid solution,  $\text{LiCr}_y\text{Mn}_{2-y}\text{O}_4$  has been studied by molecular dynamics (MD) and extended X-ray absorption fine structure (EXAFS), respectively. The MD simulation was carried out using a partially ionic model, and the relevant potential parameters were optimized. The simulated compositional dependence of lattice parameters and thermal expansion coefficients were found to be reproducible with experimental values. From the simulation results, the pair correlation function curve for  $\text{Mn}^{4+}-\text{O}$  in  $\text{LiMn}^{3+}\text{Mn}^{4+}\text{O}_4$  was broader than that in  $\text{LiCr}^{3+}\text{Mn}^{4+}\text{O}_4$ . This indicates that the local distortion of the lattice is suppressed by substituting a  $\text{Cr}^{3+}$  ion for a  $\text{Mn}^{3+}$  ion. Similar results were also obtained by EXAFS measurement. The force constant  $k$  derived from MD simulation increases by substituting  $\text{Cr}^{3+}$  ion for  $\text{Mn}^{3+}$  ion, and this corresponds to the strengthening of the bond between a transition metal cation and an oxide ion.

## Introduction

An increasing interest developed around  $\text{LiMn}_2\text{O}_4$  spinel oxides as the cathode material for lithium ion batteries due to its low cost, low toxicity, relatively high energy density, and so forth. However, this material shows marked capacity fade during charge–discharge cycles. To improve the cycle performance, several research groups have investigated the electrochemical properties of partially metal-substituted spinels  $\text{LiM}_y\text{Mn}_{2-y}\text{O}_4$  ( $M = \text{Al}, \text{Cr}, \text{Ga}, \text{Ti}, \text{Ge}, \text{Fe}, \text{Co}, \text{Zn}, \text{Ni}, \text{Mg}$ ).<sup>1–7</sup> From our previous reports,<sup>2</sup> the cycle performance was improved by substitution of  $\text{Co}^{3+}$ ,  $\text{Cr}^{3+}$ , and  $\text{Ni}^{2+}$  for  $\text{Mn}^{3+}$  (Figure 1). Gummow et al.<sup>3</sup> and Wakihara et al.<sup>8</sup> have pointed out that the substitution of a metal cation for Mn enhances the stability of spinels, but only limited reasons for the improvement of cycle ability by metal substitution are explained.

One solution for these problems is investigation of the crystal structure.  $\text{LiMn}_2\text{O}_4$  spinel belongs to cubic (space group  $Fd\bar{3}m$ ) with  $8\text{AB}_2\text{X}_4$  units per unit cell in which lithium ions locate at the tetrahedral 8a sites, manganese ions ( $\text{Mn}^{3+}$  and  $\text{Mn}^{4+}$ ) at the octahedral 16d sites, and oxide ions at the 32e sites. Detailed crystal structure of the partially substituted spinels,  $\text{LiM}_y\text{Mn}_{2-y}\text{O}_4$ , have been investigated mainly by diffraction technique.<sup>9</sup> In addition, these research studies revealed several structural features for the substitution. For example, low-temperature XRD showed that the phase transition due to Jahn–Teller distortion at low temperature was suppressed by  $\text{Cr}^{3+}$  substitution.<sup>10</sup> However, the diffraction techniques give only the averaged

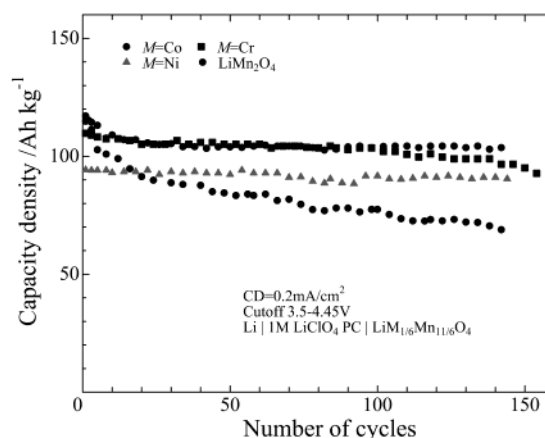


**Figure 1.** Cycle performance of  $\text{Li}/\text{LiM}_{1/6}\text{Mn}_{11/6}\text{O}_4$  ( $M = \text{Mn}, \text{Co}, \text{Cr}, \text{Ni}$ ) cell.

arrangement of ions. In other words, diffraction methods are unable to distinguish between manganese ions ( $\text{Mn}^{3+}$  and  $\text{Mn}^{4+}$ ) and doped cations ( $\text{M}^{n+}$ ), because these cations distribute randomly at the same 16d sites in the spinels  $\text{LiM}_y\text{Mn}_{2-y}\text{O}_4$ . On the other hand, molecular dynamics (MD) simulation is suitable for understanding the microscopic nature in crystals. For example, yttria-stabilized zirconia has been investigated by several researchers.<sup>11–12</sup> These research studies reveal that the local structure around the doped yttrium is important in order to understand the oxide ion conduction mechanism. The  $\text{LiMn}_2\text{O}_4$ -related materials are also investigated using MD simulation<sup>13,14</sup> and EXAFS measurement.<sup>15–17</sup> However, the local structure for metal-substituted spinel oxides,  $\text{LiM}_y\text{Mn}_{2-y}\text{O}_4$ , is not investigated yet by MD simulation.

\* Corresponding author. Tel.: +81 3 5734 2145. Fax: +81 3 5734 2146. E-mail: mwakihar@o.cc.titech.ac.jp.

<sup>†</sup> Department of Applied Chemistry, Tokyo Institute of Technology.

<sup>‡</sup> Department of Earth and Planet Science, Tokyo Institute of Technology.

In the present paper, we carry out MD simulation on chromium-doped spinels,  $\text{LiCr}_y\text{Mn}_{2-y}\text{O}_4$ , and investigate the local structure around 16d site cations,  $\text{Mn}^{3+}$ ,  $\text{Mn}^{4+}$ , and  $\text{Cr}^{3+}$ . Also, we evaluate the bond strength between transition metal cations and oxide ions by a force constant  $k$  using MD simulation.

## Methods

**Experimental Section.** The stoichiometric compounds  $\text{LiCr}_y\text{Mn}_{2-y}\text{O}_4$  ( $y = 0.0, 0.3, 0.5, 0.8, 1.0$ ) were synthesized by solid-state reactions. The reagents  $\text{Li}_2\text{CO}_3$  (99% Wako Pure Chemical Industries),  $\text{Cr}_2\text{O}_3$  (Special quality, Yoneyama Chemical Industries), and  $\text{Mn}_2\text{O}_3$  prepared by preheating of  $\text{MnCO}_3$  (99.9%, Soekawa Chemicals) at 600 °C for 48 h were used as starting materials. The mixtures were heated at 820 °C for 3 days in air, and cooled with a rate of 0.5 °C/min.

The chemical composition of each sample was evaluated by ICP measurement after dissolving the oxide with a diluted sulfuric acid. The composition obtained is equal to the ideal composition,  $\text{LiCr}_y\text{Mn}_{2-y}\text{O}_4$  within experimental error. Concerning the experimental error, we treated our samples with the formula  $\text{LiCr}_y\text{Mn}_{2-y}\text{O}_4$ . The phase identification and the evaluation of lattice parameters were carried out by a powder X-ray diffraction technique using  $\text{Cu-K}\alpha$  radiation (RINT-2500V, Rigaku Co. Ltd). Rietveld analysis was carried out for the prepared samples at room temperature using the RIETAN profile refinement program.<sup>18</sup> Divergence and scattering slits of 1/2 degree were selected and a receiving slit of 0.15 mm was chosen to attain good resolution. X-ray diffraction data for the structure refinement were collected by a step-scanning mode in the  $2\theta$  range of 20° to 120° with a step width 0.04° and a step time 2 s.

Thermal expansion was estimated from the lattice parameter in each temperature from 25 °C to 300 °C. Silicon was used as an internal standard to determine lattice parameters.

X-ray absorption measurements were carried out at the Cr and Mn K-edges. The appropriate amount of each sample powder for EXAFS measurement (determined to obtain suitable X-ray absorption) was mixed with 200 mg of boron nitride (BN) as a binder to obtain optimum absorption jump ( $\Delta\mu_{\text{t}}1$ ), and the mixture was pressed into pellets for the measurement. The data were recorded in transmission mode at the synchrotron facility, Photon-Factory, with BL-9A beam line using Si[111] double monochromators and a Rh-coated mirror for harmonic rejection. EXAFS data at the Cr K-edge were limited to 500 eV after the absorption edge (ca. 6000 eV) due to the onset of Mn absorption at ca. 6540 eV.

Fourier transformations were performed over the  $k$  range 4–14 Å<sup>-1</sup> (4–11 Å<sup>-1</sup> for Cr spectra in the substituted manganates) using  $k^3$  weighting. In this  $k$  range, the EXAFS oscillation is clear to neglect the signal/noise error. The structural parameters were determined by curve-fitting procedures using Rigaku REX2000 data analysis software.<sup>19</sup> Backgrounds were subtracted by extrapolated a Victreen-type function from the pre-edge region, and EXAFS oscillations  $\chi(k)$  were extracted using cubic spline baseline functions. Theoretical parameters used in the curve-fitting analysis were calculated by FEFF7.<sup>20</sup>

## Simulation Procedure

The interatomic potential along with a partially ionic model, i.e., the two-body central force interatomic potential terms which depend only on the position of ion pairs  $i$  and  $j$  was adopted in the present study.

The interatomic potential is expressed by

$$U_{ij} = \frac{z_i z_j e^2}{r_{ij}} + f_0(b_i + b_j) \exp\left(\frac{a_i + a_j - r_{ij}}{b_i + b_j}\right) - \frac{c_i c_j}{r_{ij}^6} + D_{ij} \{ \exp[-2\beta_{ij}(r_{ij} - r_{ij}^*)] - 2 \exp[-\beta_{ij}(r_{ij} - r_{ij}^*)] \} \quad (1)$$

The first term in eq 1 represents the Columbic interaction where  $z_i$  and  $z_j$  are the effective charges of the ions  $i$  and  $j$ , respectively, and  $r_{ij}$  is the interatomic distance between the ions. The second term represents the short-range repulsions potential. The parameters  $a_i$  and  $a_j$  reflect the ionic radii, and  $b_i$  and  $b_j$  reflect the hardness of the ions. The  $f_0$  is a constant ( $6.9478 \times 10^{-11}$  N). The third term represents the dipole-induced dipole dispersion potential based on van der Waals interaction. The last term represents the Morse potential to regard the interaction such as covalency effect. Here, we consider covalency only for the M–O bond (M = Mn, Cr).  $D_{ij}$ ,  $\beta_{ij}$ , and  $r^*$  are the specific parameters of the bond between the  $i$  and  $j$  ions.

There are so many potential parameters for MD simulation,  $Z$ ,  $a$ ,  $b$ ,  $c$ ,  $D$ ,  $\beta$ , and  $r^*$ . However, the parameters  $b$ ,  $c$ , and  $\beta$  tend to be independent of structure and to depend on the element species. These parameters were tabulated in ref 21 based on the many results of MD simulation (such as ref 22, 23). The effective charge  $Z$  is determined as follows;  $\text{Li}^+$  is known as having a high ionic character because of the low orbital energy of its 1s orbital. The ab initio calculation reported by Liu et al.<sup>24</sup> shows that the charge of  $\text{Li}^+$  in  $\text{LiMn}_2\text{O}_4$  is close to +1.0, hence the effective charge of  $\text{Li}^+$  is assigned as its full charge, +1.0. The effective charge of transition metals Mn and Cr is 55% of full charge, because previous MD simulation results applying the eq 1 model showed that the physical properties and crystal structure of transition metal oxides tend to be reproduced when the ratio of ionic character is from 50 to 60%.<sup>21–23</sup> In addition, the ab initio molecular orbital calculation for  $\text{LiMn}_2\text{O}_4$  compounds showed that the net charge of the Mn ion is 55%.<sup>24</sup> Furthermore the estimation from electronegativity data also show their amount of ionic character is about 60%.<sup>25</sup> Our preliminary MD simulation for  $\text{LiCrMnO}_4$  also shows good reproducibility of its crystal structure when the effective charges are 55%. Accordingly, the effective charges of Mn and Cr were fixed to +1.65 (55% ionicity). Finally the effective charge of oxide ion was fixed as -1.2125 by considering electrical neutrality requirement. The parameter  $r^*$  corresponds to the interatomic distance, which can be determined from the data of Shannon's ionic radii<sup>26</sup> and EXAFS results.<sup>15</sup> Hence only two parameters,  $a$  and  $D$ , need to be determined for the  $\text{LiCr}_y\text{Mn}_{2-y}\text{O}_4$  system. Both parameters were evaluated by trial and error method using the experimental data of the lattice parameter at each temperature for the end composition of the solid solution  $\text{LiCr}_y\text{Mn}_{2-y}\text{O}_4$ .

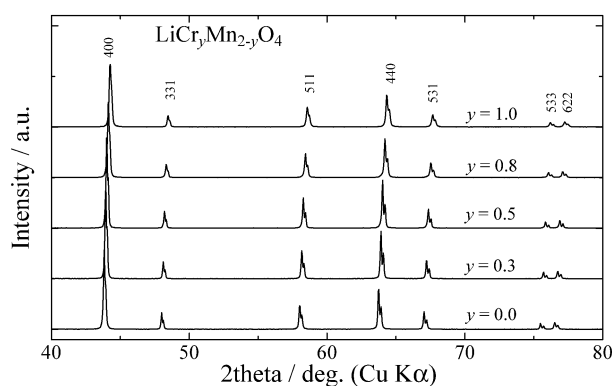
The simulation was performed using MXDORTO code developed by Kawamura.<sup>27</sup> The Verlet algorithm was used for the calculation of the atomic motions, and the Ewald method was applied for the calculations of the electrostatic interactions. The cell for the MD simulation was composed of 7000 particles ( $5 \times 5 \times 5$  unit cells), and  $\text{Mn}^{3+}$ ,  $\text{Mn}^{4+}$ , and  $\text{Cr}^{3+}$  ions are distributed randomly in the 16d sites. Periodic boundary conditions were used with the MD basic cell. The calculations were performed using the (N, P, T)-ensemble at 298 K for 15 000 steps with a time step of 2 fs. We confirm that the reproducibility of the MD simulation was confirmed by simulation with some MD cells with different distribution of  $\text{Mn}^{3+}$ ,  $\text{Mn}^{4+}$ , and  $\text{Cr}^{3+}$  in the 16d site.

**TABLE 1: Structural Parameters of  $\text{LiCr}_y\text{Mn}_{2-y}\text{O}_4$  Obtained by the Rietveld Analysis of the X-ray Diffraction Data<sup>a</sup>**

atom	site		$y = 0$	$y = 0.3$	$y = 0.5$	$y = 0.8$	$y = 1.0$
Li	8a	$(x = y = z)$	0	0	0	0	0
		B(Li)	1	1	1	1	1
M	16d	$(x = y = z)$	0.625	0.625	0.625	0.625	0.625
		B(M)	0.64(1)	0.63(1)	0.56(1)	0.41(1)	0.32(1)
O	32e	$(x = y = z)$	0.3875(5)	0.3879(2)	0.3877(2)	0.3876(2)	0.3874(2)
		B(O)	1.39(5)	1.12(5)	0.98(5)	0.72(4)	0.56(4)
		$a/\text{\AA}$	8.24528(12)	8.22703(6)	8.21317(7)	8.19768(5)	8.18879(5)
		$R_{\text{wp}}$	16.77%	13.52%	15.33%	12.98%	12.64%
		$R_p$	11.64%	9.63%	11.44%	8.71%	8.19%
		$S$	1.5214	1.3772	1.565	1.324	1.2684

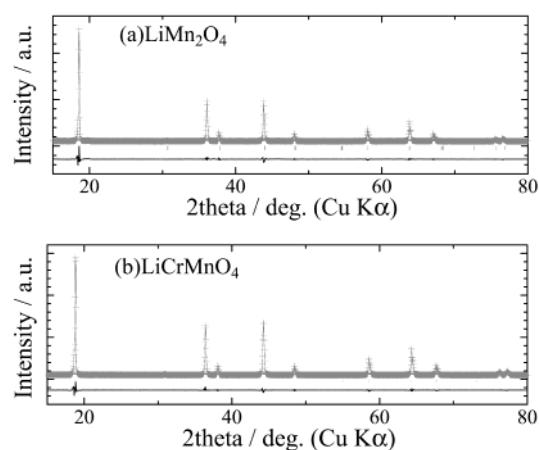
<sup>a</sup> Each refinement quality parameter is defined as follows:

$$R_{\text{wp}} = \left[ \sum_i w_i (y_{i,\text{obs}} - y_{i,\text{calc}})^2 / \sum_i w_i y_{i,\text{obs}} \right]^{1/2}, R_p = \frac{\sum_i |y_i - f_i(x)|}{\sum_i y_i}, S = \frac{R_{\text{wp}}}{R_e}$$

**Figure 2.** Powder-XRD patterns of  $\text{LiCr}_y\text{Mn}_{2-y}\text{O}_4$  ( $y = 0.0, 0.3, 0.5, 0.8, 1.0$ ).

## Results and Discussion

**Powder X-ray Diffraction.** The XRD patterns of  $\text{LiCr}_y\text{Mn}_{2-y}\text{O}_4$  ( $y = 0.0, 0.3, 0.5, 0.8, 1.0$ ) are shown in Figure 2. Under our experimental condition, the only spinel phase was observed in the composition range from  $y = 0$  to  $y = 1$ . Structure refinements of the spinel solid-solution (space group  $Fd\bar{3}m$ ) were carried out using Rietveld analysis. The arrangement of the ions in the spinel structure was fixed as follows; oxide ions were in 32e sites, Li ions were in 8a sites, and the others metal ions (Mn and Cr) were in 16d sites. The mixed-metal in the 16d site will hereinafter be termed “ $\text{M}_{16d}$ ”. The site occupancies of all the ions were also fixed at 1. The Debye–Waller coefficient  $B$  in the 8a site was fixed at  $B = 1$  because of the low scattering ability of the lithium ion, while a common  $B$  parameter was applied to all the cations in 16d sites. These assumptions are supported by the previous results on neutron diffraction.<sup>9</sup> The results of refinements are listed in Table 1, and Figure 3, parts a and b, show the final observed, calculated, and difference profiles for  $y = 0$  and  $y = 1$  samples. The lattice parameters decreased monotonically with increasing chromium content in Table 1, and the fractional coordinates of oxygen ions were almost constant at any composition  $y$ . The validity of the Rietveld analysis was supported by the relatively small refinement quality parameters,  $S$  and  $R_{\text{wp}}$  listed in Table 1, and showing a good agreement between both the calculated and experimental XRD patterns (Figure 3). Furthermore, our present results are also consistent with extrapolated data of a previously reported Rietveld analysis using neutron diffraction and XRD using a Cu  $K\alpha$  beam for the  $\text{LiMn}_{2-y}\text{Cr}_y\text{O}_4$  ( $0 \leq y \leq 1/3$ )

**Figure 3.** Rietveld refinement patterns of (a)  $\text{LiMn}_2\text{O}_4$ , and (b)  $\text{LiCrMnO}_4$  at room temperature.

spinel.<sup>9</sup> These obtained data were used as the initial structural parameters for MD simulation.

**X-ray Absorption Analysis.** It is known that the X-ray absorption near-edge structure (XANES) spectra are quite sensitive for the oxidation state and coordination environment of absorption atoms. The oxidation states and coordination environment of Mn and Cr in  $\text{LiCr}_y\text{Mn}_{2-y}\text{O}_4$  were investigated by a XANES technique. The Mn K-edge and Cr K-edge XANES spectra for  $\text{LiCr}_y\text{Mn}_{2-y}\text{O}_4$  ( $y = 0, 0.3, 0.5, 0.8, 1.0$ ) are shown in Figure 4, in comparison with those for the references  $\text{Mn}_2\text{O}_3$  and  $\text{MnO}_2$  for Mn K-edge,  $\text{Cr}_2\text{O}_3$  for Cr K-edge, respectively. These spectra consist of a pre-edge absorption (A), two steps in the absorption edge ( $B_1$  and  $B_2$ ), and two resonances above the absorption edge (C and D). These features are characteristic of the octahedral 16d site in the spinel structure.<sup>15</sup> The pre-edge peak, A, represents the transition of the 1s electron to an unoccupied 3d orbital of Cr and Mn ions.<sup>28</sup> Although the 1s to 3d transition is an electronic dipole-forbidden transition in an ideal octahedral symmetry, the appearance of the weak absorption peak is due to pure electronic quadruple coupling and the noncentrosymmetric environment of the slightly distorted  $\text{MO}_6$  ( $\text{M} = \text{Cr}^{3+}, \text{Mn}^{3+}$ ; trivalent cations) octahedral site. The intensity of peak A of  $\alpha\text{-MnO}_2$  in Mn K-edge XANES is larger than that of  $\text{LiCr}_y\text{Mn}_{2-y}\text{O}_4$  because  $\alpha\text{-MnO}_2$  has rutile structure ( $P4_2/mnm$ ) and the  $\text{MnO}_6$  octahedra was distorted. The main peak, B and C, represents the electron transfer from 1s to 4p.<sup>28</sup> The shapes of both Mn K-edge and Cr

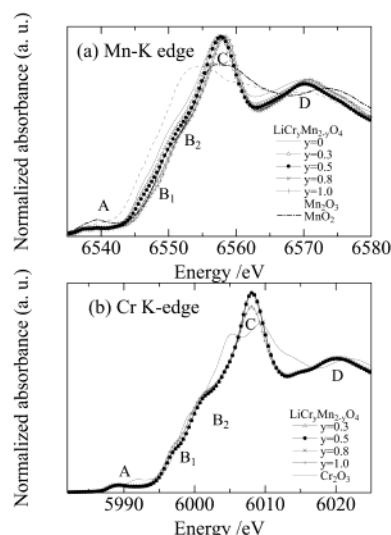


**Figure 4.** XANES spectra for (a) Mn K-edge and (b) Cr K-edge of  $\text{LiCr}_y\text{Mn}_{2-y}\text{O}_4$ .

**TABLE 2: Optimized Parameters of Each Ion and Ion Pair for MD Simulation**

ion	$z$ $e$	$a$ $\text{\AA}$	$b$ $\text{\AA}$	$c$ $(\text{kJ mol}^{-1})^{1/2} \text{\AA}^{-3}$
$\text{Li}^+$	1.0000	1.0010	0.08	1.64
$\text{Mn}^{3+}$	1.6500	0.8519	0.10	0.00
$\text{Mn}^{4+}$	2.2000	0.8189	0.10	0.00
$\text{Cr}^{3+}$	1.6500	0.9328	0.10	0.00
$\text{O}^{2-}$	-1.2125	1.9265	0.18	40.91

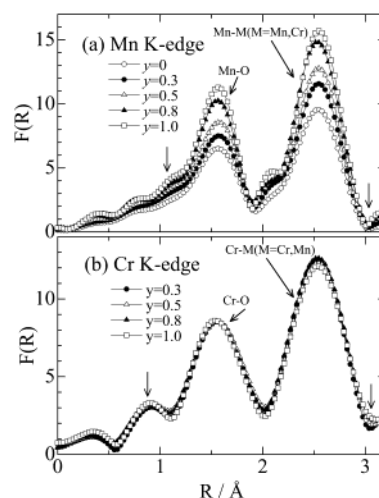
  

ion pair	$D$ $\text{kJ mol}^{-1}$	$\beta$ $\text{\AA}^{-1}$	$r^*$ $\text{\AA}$
$\text{Mn}^{3+}-\text{O}$	9.53	2.00	2.10
$\text{Mn}^{4+}-\text{O}$	12.21	2.00	2.00
$\text{Cr}^{3+}-\text{O}$	15.39	2.00	1.99

K-edge spectra remained unchanged with composition  $y$ . Therefore it is concluded that the Mn and Cr ions may reside in the octahedral 16d site. In the Mn K-edge XANES spectra, the absorption edges were shifted to higher energy with increasing Cr content. This shift is correlated with an increase to over 3.5+ in the Mn oxidation state by Cr substitution, as expected if Cr ions replace trivalent Mn ions. Cr K-edge XANES spectra are quite similar for various  $y$  values in  $\text{LiCr}_y\text{Mn}_{2-y}\text{O}_4$ , which means the Cr oxidation state is not changed with an increase in Cr content. Accordingly, the experimental results of the oxidation state consisted with our MD simulation model listed in Table 2, where the oxidation state of Cr is unchanged, and that of Mn varied with Cr doping to keep electroneutrality.

Fourier-transformed (FT) of EXAFS oscillations for Cr and Mn K-edges are shown in Figure 5. The obtained bond length in the figure showed it to be quite small from the data of ionic radii,<sup>26</sup> because phase-shift corrections have not been applied to the FT spectra. The first two intense peaks around 1.5 and 2.5  $\text{\AA}$  in the Fourier-transformed data result from simple backscattering of the photoelectron from the first coordination shell of six oxygen atoms and the second coordination shell of cations occupying the six neighboring 16d octahedral sites.

The peak intensity and broadness of FT spectra correlate to the coordination number (CN) and Debye–Waller factors which reflects the thermal reflection and/or distortion of bonds. Since the CN with composition  $y$  for absorption atom and the experimental temperature unchanged in this experiment, the changes of peak intensity mainly depend on the distortion of



**Figure 5.** EXAFS spectra for (a) Mn and (b) Cr K-edge of  $\text{LiCr}_y\text{Mn}_{2-y}\text{O}_4$ .

$\text{MO}_6$  ( $M = \text{Cr}$  and  $\text{Mn}$ ) octahedra. Figure 5 shows that with an increase in the Cr content, the intensity of the FT spectra of Mn K-edge increased, while that of Cr K-edge remained unchanged. Therefore the local distortion around Mn ions was depressed by introducing the Cr ions. Similar results were shown by Ammudsen et al.<sup>15</sup> However, such depression is only observed around Mn ions, not around Cr ions.

To estimate the local structural distortion more quantitatively, accurate structural information concerning the nearest oxygen and cation neighbors was obtained by curve-fitting to the experimental data Fourier-filtered over the first two peaks in the transformation. The structural parameters obtained by curve-fitting are summarized in Table 3. The splitting in Mn–M and Mn–O spectra are not seen even in  $\text{LiMn}_2\text{O}_4$ . Therefore, in this fitting procedure, we fixed the CN of Mn(Cr)–O and Mn(Cr)–M as 6 ( $M = \text{Mn}$  and  $\text{Cr}$ ). Considering the local structural description, the bond lengths for Cr–Cr, Cr–Mn, and Mn–Mn are different from one another. Therefore the peaks due to the second neighbor interaction (assigned as Cr–M, or Mn–M) shown in Figure 5 should separate into more than two peaks. However, because of the limitation of experimental resolution, only a single peak is observed. In this curve-fitting procedure, the second shell's interaction was treated as the bond which has averaged interatomic distance between the absorber atom Cr or Mn and the scattered atom  $M (= \text{Cr}, \text{Mn})$ . The Cr–M indicates the averaged contribution of the interaction Cr–Cr and Cr–Mn, and the Mn–M is that of the interaction Mn–Cr and Mn–Mn, respectively. The bond lengths of the first and second neighbor ions around Mn or Cr ions were slightly decreased with doping Cr ion. It is also found that the Debye–Waller factors which correspond to the local distortion of each Mn–O and Mn–M bond for Mn K-edge spectra are decreased with an increase of the Cr content. On the other hands, this is not observed in Cr K-edge spectra. These results indicate the depression of the local distortion of the lattice around Mn ions as mentioned above.

## Molecular Dynamics Simulation

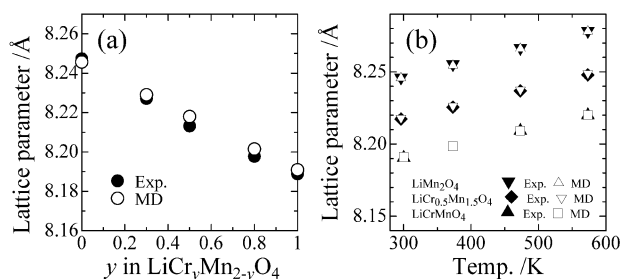
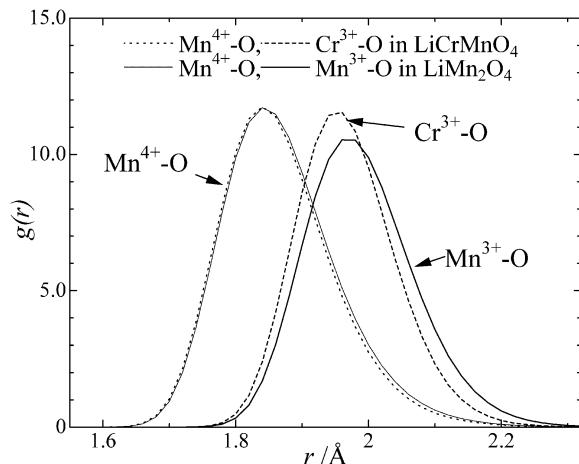
**Local Structure of  $\text{LiCr}_y\text{Mn}_{2-y}\text{O}_4$ .** The potential parameters were optimized by the composition dependence of lattice parameters and thermal expansion coefficients, and the potential parameters obtained are listed in Table 2. The compositional dependence of the lattice parameters and the thermal expansion coefficients of  $\text{LiMn}_2\text{O}_4$  and  $\text{LiCrMnO}_4$  obtained by the MD



**TABLE 3: Mn K-edge and Cr K-edge EXAFS Determined Structural Parameters, Coordination Number (CN), Bond Length (R), Debye–Waller Factors (–), for the Cr-Substituted Lithium Manganates,  $\text{LiCr}_y\text{Mn}_{2-y}\text{O}_4$  ( $y = 0, 0.3, 0.5, 0.8, 1.0$ )**

	Mn–O			Mn–M			residue (%)	Cr–O			Cr–M			residue (%)
	CN <sup>a</sup>	R/Å	$\sigma$ /Å	CN <sup>a</sup>	R/Å	$\sigma$ /Å		CN <sup>a</sup>	R/Å	$\sigma$ /Å	CN <sup>a</sup>	R/Å	$\sigma$ /Å	
$\text{LiMn}_2\text{O}_4$	6	1.917	0.074	6	2.916	0.061	3.249	6	–	–	6	–	–	–
$\text{LiCr}_{0.3}\text{Mn}_{1.7}\text{O}_4$	6	1.918	0.069	6	2.913	0.052	3.613	6	1.990	0.070	6	2.928	0.051	3.927
$\text{LiCr}_{0.5}\text{Mn}_{1.5}\text{O}_4$	6	1.914	0.065	6	2.906	0.051	3.067	6	1.987	0.069	6	2.925	0.051	3.350
$\text{LiCr}_{0.8}\text{Mn}_{1.2}\text{O}_4$	6	1.911	0.055	6	2.901	0.040	3.949	6	1.981	0.066	6	2.921	0.047	2.604
$\text{LiCrMnO}_4$	6	1.908	0.047	6	2.898	0.035	3.087	6	1.980	0.062	6	2.919	0.048	2.470

<sup>a</sup> Fixed parameter for the curve-fitting procedure, residue =  $\{\sum [k^3\chi_{\text{obs}}(k) - k^3\chi_{\text{calc}}(k)]^2\} / \{\sum [k^3\chi_{\text{obs}}(k)]^2\}$ .

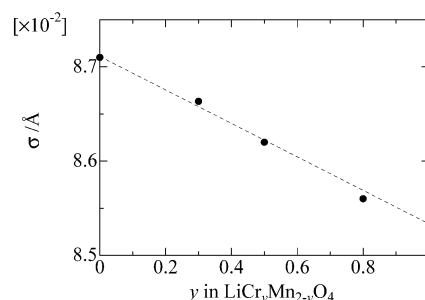
**Figure 6.** (a) Lattice parameter dependence of  $y$  in  $\text{LiCr}_y\text{Mn}_{2-y}\text{O}_4$ . (b) Lattice parameter dependence of temperature in  $\text{LiCr}_y\text{Mn}_{2-y}\text{O}_4$ .**Figure 7.** pcf between metal and oxide ions in  $\text{LiMn}_2\text{O}_4$  and  $\text{LiCrMnO}_4$ .

simulation are shown in Figure 6, parts a and b, respectively, together with the experimental value. As shown in this figure, the potential parameters for MD simulation are well reproducible to the experimental data.

To investigate the microscopic structure, the pair correlation functions (pcf),  $g_{ij}(r)$  of  $\text{M}_{16d}\text{--O}$  in both  $\text{LiMn}_2\text{O}_4$  and  $\text{LiCrMnO}_4$  were calculated using the following equation:

$$g_{ij}(r) = \frac{n_{ij}(r)}{4\pi(N_i N_j / V) r^2 \Delta r} \quad (2)$$

where  $N_i$  and  $N_j$  are the number of ions in the basic cell with volume  $V$ ,  $n_{ij}(r)$  is the number of the pair of ion  $i$  and ion  $j$  between the distance of  $r - (\Delta r/2)$  and  $r + (\Delta r/2)$  where  $\Delta r$  is 1 pm. The results of calculated pcf at 298 K are shown in Figure 7. The peak top of each pcf curve relates to the bond length of M–O. In the bond length of M–O, there are following relations:  $\text{Mn}^{3+}\text{--O} > \text{Cr}^{3+}\text{--O} > \text{Mn}^{4+}\text{--O}$ . This behavior can be understood from the ionic radii because the relation of the ionic radii is  $\text{Mn}^{3+}(0.785 \text{ Å (high spin)})^{26} > \text{Cr}^{3+}(0.755 \text{ Å})^{26} > \text{Mn}^{4+}(0.670 \text{ Å})^{26}$ .  $\text{Mn}^{4+}\text{--O}$  distances in both  $\text{LiMn}_2\text{O}_4$  and

**Figure 8.** The variation of standard deviation in the pcf curves of  $\text{Mn}^{4+}\text{--O}$  with the composition  $y$  in  $\text{LiCr}_y\text{Mn}_{2-y}\text{O}_4$ .

$\text{LiCrMnO}_4$  were quite similar, while the  $\text{Cr}^{3+}\text{--O}$  distance is shorter than that in  $\text{Mn}^{3+}\text{--O}$ . This behavior could be understood from the idea of ionic radius, i.e., the  $\text{Cr}^{3+}$  ion has relatively smaller ionic radii ( $0.755 \text{ Å}^{26}$ ) than that of  $\text{Mn}^{3+}$  ion ( $0.785 \text{ Å}^{26}$ ). The standard deviation of pcf for  $\text{Mn}^{4+}\text{--O}$  is shown in Figure 8, where we can see that the peak width for  $\text{Mn}^{4+}\text{--O}$  decreases with  $y$  in  $\text{LiCr}_y\text{Mn}_{2-y}\text{O}_4$ . The increasing standard deviation of each peak is caused by the thermal oscillation and geometrical structural distortion. The MD simulations with various compositions of  $y$  were done at the same temperature, 298 K, so that there are not so much difference of thermal oscillation effect. Therefore, the decrease of the standard deviation means the depression of geometrical distortion in the lattice. From Figure 7, the bond length of  $\text{Cr}^{3+}\text{--O}$  is closer to that of  $\text{Mn}^{4+}\text{--O}$  than in the case of  $\text{Mn}^{3+}\text{--O}$  and  $\text{Mn}^{4+}\text{--O}$ , hence, replacement of  $\text{Mn}^{3+}$  by  $\text{Cr}^{3+}$  results in the homogeneous distribution of the M–O bond length. Therefore these calculated results lead to the fact that the octahedron of  $\text{Mn}^{4+}\text{--O}_6$  in  $\text{LiMn}_2\text{O}_4$  is much more distorted compared with that in  $\text{LiCr}_y\text{Mn}_{2-y}\text{O}_4$ . This distortion might be increased by the mismatch of ionic radii, because the difference of the ionic radii between  $\text{Mn}^{3+}(0.785 \text{ Å})$  and  $\text{Mn}^{4+}(0.670 \text{ Å})$  is larger than the difference between  $\text{Cr}^{3+}(0.755 \text{ Å})$  and  $\text{Mn}^{4+}$ .

As mentioned above, the local distortion of  $\text{LiMn}_2\text{O}_4$  would be suppressed by introducing chromium ions. To confirm these phenomena on the atomic scale, we focus on the O–M–O bond in the octahedral network in spinel oxides. Figure 9 shows a part of octahedral networks extracted arbitrarily from the MD cell that consists of two trivalent cations and one tetravalent cation in 16d sites, and adjacent oxide anions in 32e site. If these sites are equivalent in view of crystallography, the bond angle (from  $(\alpha)$  to  $(\delta)$  in Figure 9) should be equal. Figure 10, parts a and b, show the variation of the simulated O–M–O bond angle for 2000 fs. The average value of  $(\gamma)$  and  $(\delta)$  is similar in the both compounds, and this should be caused by the same ionic radii of adjacent cation pairs. On the other hand, the bond angle  $(\alpha)$  and  $(\beta)$  is different, and this indicates the distortion of an octahedron arising from the adjacent  $\text{M}^{4+}$  and  $\text{M}^{3+}$  cation pair which has a large difference in ionic radii. In addition, the difference of the bond angle  $(\alpha)$  and  $(\beta)$  in

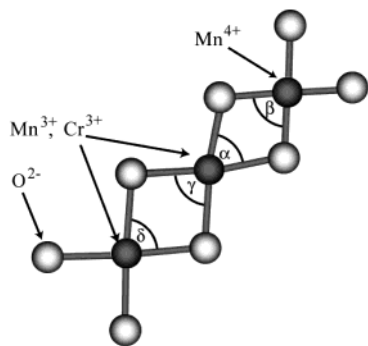


**Figure 9.** Schematic figure for the local O–M–O bond angles ( $\alpha$ ), ( $\beta$ ), ( $\gamma$ ) and ( $\delta$ ).

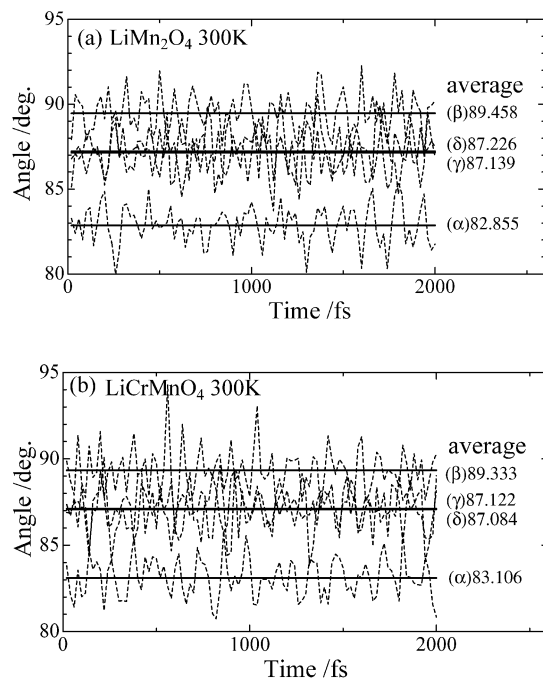


**Figure 10.** The time dependence of each O–M–O bond angle of (a)  $\text{LiMn}_2\text{O}_4$  and (b)  $\text{LiCrMnO}_4$ .

$\text{LiMn}^{3+}\text{Mn}^{4+}\text{O}_4$  is larger than that in  $\text{LiCr}^{3+}\text{Mn}^{4+}\text{O}_4$ . Accordingly it was concluded that  $\text{Cr}^{3+}$  substitution for  $\text{Mn}^{3+}$  leads to a decrease in the local distortion of the octahedron  $\text{M}^{3+}\text{O}_6$ . These results of local distortion in lithium manganese spinels agree with that for EXAFS analysis. Therefore it is considered that the MD simulation confirms the experimental data on the local structure.

**$\text{M}_{16d}$ –O Bond Strength in  $\text{LiCr}_y\text{Mn}_{2-y}\text{O}_4$ .** We investigated the bond strength by analyzing the lattice energy change with displacement of the  $\text{M}^{3+}$  ion by MD simulation. Figure 11 shows the variation of lattice energy with  $\text{M}^{3+}$  displacement from the crystallographic 16d site along the [100], [110], [111] direction.

According to the harmonic oscillation theory, the vibration of 2 atoms ( $i$  and  $j$ ) is expressed by following equation:

$$U_{ij} = \frac{1}{2}kx^2 \quad (3)$$

where  $U_{ij}$  indicates the potential energy,  $k$  means force constant of the bond, and  $x$  means the displacement of atom from equilibrium position, or the minimum value point of potential energy. This equation can apply to the crystal structure.

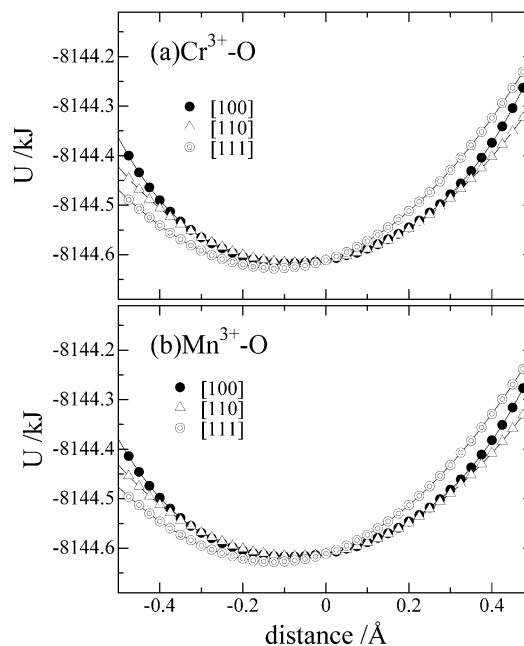


**Figure 11.** The variation of lattice energy with displacement of  $\text{M}^{3+}$  ((a)  $\text{M} = \text{Cr}$ , (b)  $\text{M} = \text{Mn}$ ) in  $\text{LiCr}_{0.5}\text{Mn}_{1.5}\text{O}_4$ .

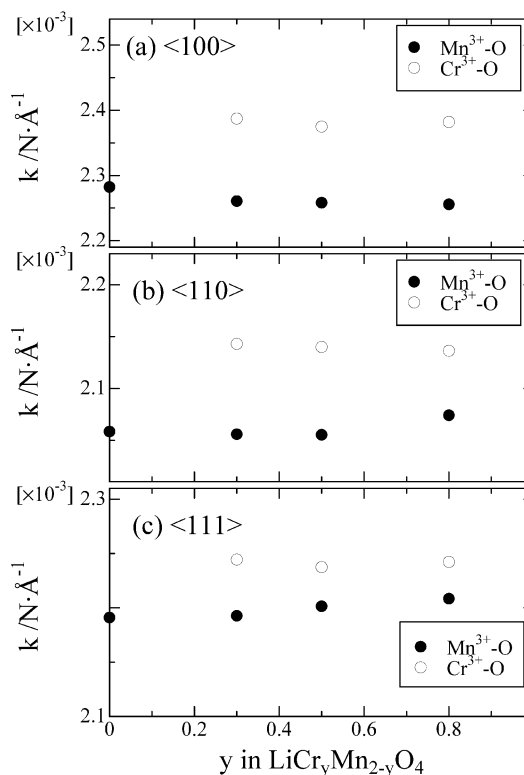


**Figure 12.** The force constant for each direction ((a)  $\langle 100 \rangle$ , (b)  $\langle 110 \rangle$ , and (c)  $\langle 111 \rangle$ ) with  $y$  in  $\text{LiCr}_y\text{Mn}_{2-y}\text{O}_4$ .

However, actually this equation can only apply to the quite small  $x$  values. Actual energy curves can be approximated more exactly by adding an anharmonic term as in the following equation:<sup>29</sup>

$$U(x) = \frac{1}{2}kx^2 - gx^3 - fx^4 \quad (4)$$

In this equation,  $k$ ,  $g$ , and  $f$  are positive constants,  $-gx^3$  means asymmetric interaction of repulsive force with atoms, and  $-fx^4$

means the softness of vibration due to large displacement. Figure 12 shows the compositional dependence on the force constant  $k$  for each direction ( $\langle 100 \rangle$ ,  $\langle 110 \rangle$ ,  $\langle 111 \rangle$ ), and the  $k$  values of  $\text{Cr}^{3+}-\text{O}$  are larger than those of  $\text{Mn}^{3+}-\text{O}$  in all the composition  $y$ . In the other words, the  $\text{Cr}^{3+}-\text{O}$  bond is stronger than  $\text{Mn}^{3+}-\text{O}$ . It shows that the strength of  $\text{Mn}^{3+}-\text{O}$  and  $\text{Cr}^{3+}-\text{O}$  are not changed with chromium contents. Since the amount of the  $\text{Cr}^{3+}-\text{O}$  bond increases with composition  $y$ , the  $\text{MO}_6$  octahedra in  $\text{LiCr}_y\text{Mn}_{2-y}\text{O}_4$  may be more rigid than that in  $\text{LiMn}_2\text{O}_4$ . Accordingly, this is one of the possible reasons for the improvement of cycleability in substituted spinels as mentioned in the Introduction section.

## Conclusion

Local structure in chromium-doped lithium manganese oxide ( $\text{LiCr}_y\text{Mn}_{2-y}\text{O}_4$ ) was investigated by means of molecular dynamics simulation and EXAFS analysis. Obtained potential parameters for MD simulation are reproducible for the lattice parameters at room temperature and thermal expansion coefficients. From the MD simulation for  $\text{LiMn}^{3+}\text{Mn}^{4+}\text{O}_4$  and  $\text{LiCr}^{3+}\text{Mn}^{4+}\text{O}_4$ , the calculated results show that the distortion of  $\text{MO}_6$  octahedra decreases with chromium doping. Similar results were also obtained from EXAFS data. It suggests that local distortion is caused by the difference of ionic radii in adjacent cation pairs. From the analysis of the site potential around the octahedral cation site using optimized data from MD simulation, it is clear that the substitution by  $\text{Cr}^{3+}$  for  $\text{Mn}^{3+}$  strengthened the bond between  $\text{M}_{16d}$  and O atoms.

The improvement of the cycle ability in many partially substituted  $\text{LiM}_y\text{Mn}_{2-y}\text{O}_4$  for lithium secondary batteries may be attributed to the strengthening of the bond between the transition metal cation and the oxide ion by substituting a  $\text{Cr}^{3+}$  ion for a  $\text{Mn}^{3+}$  ion.

**Acknowledgment.** This work was supported by Grant-in-Aid for Scientific Research on Priority Areas (B) (No.740) "Fundamental Studies for Fabrication of All Solid State Ionic Devices" from Ministry of Education, Culture, Sports, Science and Technology. The Mn K-edge and Cr K-edge XAFS experiments were performed at the Photon Factory with the approval of the High Energy Accelerator Research Organization (Proposal No. 2001G120).

## References and Notes

- (1) Bittihn, R.; Herr, R.; Hoge, D. *J. Power Sources* **1993**, 43–44, 223.
- (2) Guohua, Li; Ikuta, H.; Uchida, T.; Wakihara, M. *J. Electrochem. Soc.* **1996**, 143, 178.
- (3) Gummow, R. J.; Kock, A. de; Thackeray, M. M. *Solid State Ionics* **1994**, 69, 59.
- (4) Robertson, A. D.; Lu, S. H.; Averill, W. F.; Howard, W. F., Jr. *J. Electrochem. Soc.* **1997**, 144, 3500.
- (5) Robertson, A. D.; Lu, S. H.; Howard, W. F., Jr. *J. Electrochem. Soc.* **1997**, 144, 3505.
- (6) Cras, F. Le; Bloch, D.; Anne, M.; Strobel, P. *Solid State Ionics* **1996**, 89, 203.
- (7) Pistoia, G.; Wang, G. *Solid State Ionics* **1993**, 66, 135.
- (8) Wakihara, M.; Guohua, Li; Ikuta, H. *Lithium Ion Batteries*; Kodansha: New York, 1998; Chapter 2.
- (9) Oikawa, K.; Kamiyama, T.; Izumi, F.; Nakazato, D.; Ikuta, H.; Wakihara, M. *J. Solid State Chem.* **1999**, 146, 322.
- (10) Ikuta, H.; Takanaka, K.; Wakihara, M. *Solid State Ionics*, submitted.
- (11) Shimajo, F.; Okabe, T.; Tachibana, F.; Kobayashi, M.; Okazaki, H. *J. Phys. Soc. Jpn.* **1992**, 61, 2848.
- (12) Li, X.; Hafskjold, B. *J. Phys.: Condens. Mater.* **1995**, 7, 1255.
- (13) Ammundsen, B.; Roziere, J.; Islam, M. S. *J. Phys. Chem. B* **1997**, 101, 8156.
- (14) Ammundsen, B.; Burns, G. R.; Islam, M. S.; Kanoh, H.; Roziere, J. *J. Phys. Chem. B* **1999**, 103, 5175.
- (15) Ammundsen, B.; Jones, D. J.; Roziere, J. *J. Phys. Chem. B* **1998**, 102, 7939.
- (16) Nakai, I.; Yasaka, K.; Sasaki, H.; Terada, Y.; Ikuta, H.; Wakihara, M. *J. Power Sources* **2001**, 97, 412.
- (17) Aitchison, P.; Ammundsen, B.; Jones, D. J.; Burns, G.; Roziere, J. *J. Mater. Chem.* **1999**, 9, 3125.
- (18) Kim, Y.; Izumi, F. *J. Ceram. Soc. Jpn.* **1994**, 102 (4), 401.
- (19) Rigaku EXAFS Analysis Software, REX2000, Catal. No. 2612S211, Rigaku Co., 1996. Rigaku International Corp. 3-9-12, Matsubara-cho, Akishima-shi, Tokyo 196, Japan.
- (20) Ankudinov, A. L.; Ravel, B.; Rehr, J. J.; Conradson, S. D. *Phys. Rev. B* **1998**, 58, 7565.
- (21) Hirao, K.; Kawamura, K. *Material Design using Personal Computer*; Shokabo, Tokyo, 1994.
- (22) Katsumata, T.; Inaguma, Y.; Itoh, M.; Kawamura, K. *Solid State Ionics* **1998**, 108, 175.
- (23) Katsumata, T.; Inaguma, Y.; Itoh, M.; Kawamura, K. *J. Ceram. Soc. Jpn.* **1999**, 625, 107.
- (24) Liu, Y.; Fujiwara, T.; Yukawa, H.; Morinaga, M. *Electrochim. Acta* **2001**, 46, 1151.
- (25) Pauling, L. *The Nature of Chemical Bond*; Cornell University Press: New York, 1960.
- (26) Shannon, R. D. *Acta Crystallogr.* **1976**, A32, 751.
- (27) Kawamura, K. MXDORTO, Japan Chemistry Program Exchange, #029.
- (28) Park, H. S.; Hwang, S. J.; Choy, J. H. *J. Phys. Chem. B* **2001**, 105, 4860.
- (29) Kittel, C. *Introduction to Solid State Physics*; Wiley: New York, 1996; Chapter 4.